APL Materials

Photonic memory with nonlinear plasmonic nanotubes

Cite as: APL Mater. 9, 101111 (2021); https://doi.org/10.1063/5.0056049
Submitted: 06 May 2021 • Accepted: 18 September 2021 • Published Online: 12 October 2021

Aivar Abrashuly and Constantinos Valagiannopoulos

COLLECTIONS

Paper published as part of the special topic on Light and Matter Interactions

View Online Export Citation CrossMark

ARTICLES YOU MAY BE INTERESTED IN

Spin–orbit torques of an in-plane magnetized system modulated by the spin transport in the ferromagnetic Co layer
APL Materials 9, 101106 (2021); https://doi.org/10.1063/5.0048917

Automatic design#of chiral mechanical metamaterials
APL Materials 9, 101112 (2021); https://doi.org/10.1063/5.0066210

Homoepitaxial β-Ga_2O_3 transparent conducting oxide with conductivity σ = 2323 S cm^{-1}
APL Materials 9, 101105 (2021); https://doi.org/10.1063/5.0062056

Submit Today!
APL Materials
SPECIAL TOPIC: Design, Material, Function, and Fabrication of Metamaterials

AIP Publishing

© 2021 Author(s).

Photonic memory with nonlinear plasmonic nanotubes

Cite as: APL Mater. 9, 101111 (2021); doi: 10.1063/5.0056049
Submitted: 6 May 2021 • Accepted: 18 September 2021 •
Published Online: 12 October 2021

View Online Export Citation CrossMark

Aivar Abrashuly[1,2] and Constantinos Valagiannopoulos[2,a)]

AFFILIATIONS

[1] Department of Electrical Engineering, Stanford University, Stanford, California 94305, USA
[2] School of Sciences and Humanities, Nazarbayev University, Nur-Sultan KZ-010000, Kazakhstan

Note: This paper is part of the Special Topic on Light and Matter Interactions.
[a)] **Author to whom correspondence should be addressed:** konstantinos.valagiannopoulos@nu.edu.kz

ABSTRACT

Photonic memory devices are capable of giving different outputs for the same present input, judging from the input's past values and, in this way, "remembering" what happened the previous times. Nonlinear cylindrical metasurfaces, when fed centrally by line sources of various angular momenta, are found to possess exactly this property, which is called multistability; in particular, they can develop multiple responses in proportion to what the history of excitation intensities is. Interestingly, some of the potential radiation patterns of the considered nanotubes, despite the homogeneous and isotropic nature of the structure, are azimuthally rotated, even for symmetric excitations. Such a feature of several alternative stable solutions with different amplitudes and angular tilts may provide a promising route for designing reconfigurable optical setups with versatile memory and storage utilities.

© 2021 Author(s). All article content, except where otherwise noted, is licensed under a Creative Commons Attribution (CC BY) license (http://creativecommons.org/licenses/by/4.0/). https://doi.org/10.1063/5.0056049

I. INTRODUCTION

Nonlinearities are present in practically any photonic substance as long as the local field magnitudes are suitably large to substantially modify the effective properties of the media.[1] Such intensity-dependent features inherit enriched and versatile dynamics to the corresponding systems and make them able to host counter-intuitive effects[2] and manipulate electromagnetic fields.[3] Fascinating applications such as the precise control of high-field interactions in laser oscillators[4] or strong light confinement[5] and intense focusing[6] in photonic crystals nanocavities have become feasible only because of the nonlinear response of the utilized materials. Under harmonic excitation, the constituent relations describing such a response are oscillating too, and thus, higher-order harmonics are generated, allowing for efficient frequency mixing[7] and all-optical light modulation.[8] Importantly, devices exploiting nonlinearities such as photonic sensors using silicon,[9] optical switches[10] or limiters that integrate plasmonics,[11] and tunneling waveguides comprising near-zero index media[12] are expected to become ubiquitous and affordable for mass production in the near future.

One of the most important applications associated with nonlinear setups concerns the ability to modify the output judging not only from the current level of their inputs but also from their history, namely, making efficient photonic memory components. Their principle of operation is related to the supported phase changes by the incorporated media such as metalloid alloys,[13] organic films,[14] composite nanoparticles,[15] or simply isolated elements.[16] That switch in the response can permanently modify the crystalline texture and lead to the design of storage cells that can retain stored information even after power is removed[17] such as non-volatile architectures that can be programmed with a single pulse regardless of the previous state of the material.[18] Furthermore, metasurfaces comprising arrays of film-coupled nanopatches have been both designed[19] and fabricated[20] and are found to possess substantial bistability in the reflection of various diffraction orders. Finally, memory elements are based on nonlinear operation even though they do not concern electromagnetic response but involve other effects such as quantum scattering,[21] neuronal activity,[22] or optothermal interplay.[23]

Cylindrical geometries, being amenable to analytical treatment, are particularly suitable for investigating nonlinear interactions with light. In particular, chemically synthesized nanowires offer a unique material platform[24] for producing photonic elements, including beam formers,[25] anomalous scatterers,[26] and all-optical signal processors.[27] Multilayered nanorods have also been examined[28] to achieve plasmonic bistability for the propagating modes, an effect that has been significantly enhanced by non-local cores.[29]

Importantly, several approximate solutions have been proposed for studying cylindrical configurations with nonlinear features from quasi-phase-matching in resonators[30] to discretization of cross sections[31] and iterative scattering corrections[32] in isolated wires.

In this work, we consider a nanotube characterized by surface impedance with Kerr nonlinearity that is centrally excited by a line source. Once its field is omni-directional, the problem is analytically solvable, and ordinary bistability is recorded. In case the feeding source has a dipolar pattern, a nonlinear set of two equations is obtained, and the steady-state transmissivity pattern is approximately determined by dropping the higher orders of angular momentum. The obtained solution does not always respect the symmetry of the excitation. In particular, several solution branches are identified, leading to the emergence of multistabilities, and importantly, parts of the sets of roots give rotated radiation profiles that further enrich the potential of the device as electromagnetic memory cell. All these combinations of input intensity, solution type, and output power make a versatile phase space, exceptionally befitting to a variety of memory-related applications from reconfigurable beam steering and dynamic displays to tunable photonic tagging, information storage, and encrypted optical communications.

II. MATHEMATICAL FORMULATION

A. Omni-directional excitation

Let us consider a cylindrical metasurface of radius a, as depicted in Fig. 1, where the employed Cartesian (x, y, z) and cylindrical (r, φ, z) coordinate systems are also defined. The surface admittance σ comprises a linear part $i\gamma$ and is characterized by Kerr nonlinearity with coefficient κ. The structure exists into vacuum and is excited internally by an electric current line source of wavelength λ, producing an omni-directional excitation pattern of electric field amplitude $E_0 > 0$ at $r = a$. Since both the excitation and the structure are not dependent on the z variable, the electric field is always and in all areas parallel to the z axis, and thus, $\mathbf{E} = \hat{\mathbf{z}}E$. For brevity, we assume a lossless structure, and thus, the surface admittance σ is purely imaginary; as a result, both γ and κ are taken as real. With the suppressed harmonic time dependence ($e^{+i\omega t}$, where ω is the adopted angular frequency), in case the nanotube is of dielectric nature (relative permittivity $\varepsilon > 1$), and we have $\mathrm{Im}[\sigma] > 0$, and if it is plasmonic ($\varepsilon < 1$), we have $\mathrm{Im}[\sigma] < 0$.

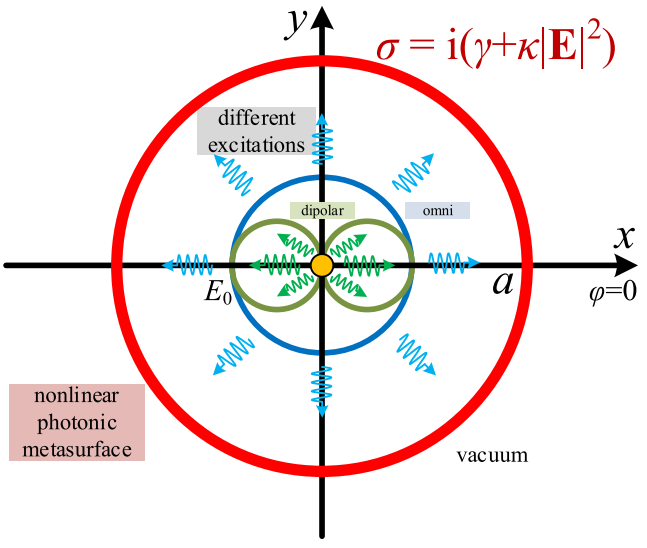

FIG. 1. Indicative sketch of the investigated configuration. A circular cylindrical metasurface of radius a and surface admittance σ having a linear part γ and Kerr coefficient κ is excited centrally by line sources possessing either an omni-directional or bipolar angular profile. Our mission will be to examine the multistability of its radiation pattern and test its ability to work as a photonic memory nanotube. The amplitude of the electric field is denoted by $E_0 > 0$.

The incident electric field is expressed as $E_{inc} = E_0 \frac{H_0(k_0 r)}{H_0(k_0 a)}$ while the transmissive component (for $r > a$) is written in the form $E_{tran} = E_0 T \frac{H_0(k_0 r)}{H_0(k_0 a)}$, where $k_0 = 2\pi/\lambda$ is the free-space wavenumber, T the dimensionless complex transmission coefficient, and H_n is the second-type Hankel function of n-th order. If one applies the boundary conditions at $r = a$ for continuity of electric field and discontinuity of magnetic field by the effective surface current σE, the following cubic equation with respect to transmissivity $\tau = |T|^2$ is derived,

$$\left[1 + F_0^2\left(\gamma\eta_0 + \tau\,\kappa\eta_0 E_0^2\right)^2\right]\tau = 1, \tag{1}$$

where $\eta_0 = 120\,\Omega$ is the wave impedance into vacuum and $F_n = \frac{\pi k_0 a}{4}|H_n(k_0 a)|^2$. Such an equation as (1) can be analytically solved, and the acceptable solutions $0 < \tau < 1$ can be collected. The transmissivity τ cannot surpass unity, as indicated by (1), given the fact that both γ and κ are real. It should also be stressed that the linear solution is readily found for $\kappa = 0$ as $\tau = \frac{1}{1+(\gamma\eta_0)^2 F_0^2}$.

B. Dipolar excitation

If the angular pattern of the incident field is dipolar,[33] as indicated by Fig. 1, that is, $E_{inc} = E_0 \frac{H_1(k_0 r)}{H_1(k_0 a)} \cos\varphi$, we can assume that the transmission possesses the form $E_{tran} = E_0 \frac{H_1(k_0 r)}{H_1(k_0 a)}\left[T_+ e^{+i\varphi} + T_- e^{-i\varphi}\right]$, where (T_+, T_-) are the dimensionless transmission coefficients. Note that we let the transmissivity be non-symmetric $(T_+ \neq T_-)$ due to the nonlinearity of the metasurface, which excites additional angular harmonics $e^{in\varphi}$.

We impose the same boundary conditions as in Subsection II A, but the inhomogeneous one referring to the magnetic field is now applied only approximately by keeping only the dipolar terms $e^{\pm i\varphi}$. After expressing the real and imaginary parts of the transmission coefficients (T_+, T_-) in terms of the transmissivities $\tau_\pm = |T_\pm|^2$, we obtain the following 2×2 system of nonlinear coupled equations:

$$\left\{1 + F_1^2\left[\gamma\eta_0 + (\tau_+ + 2\tau_-)\kappa\eta_0 E_0^2\right]^2\right\}\tau_+ = 1, \tag{2}$$

$$\left\{1 + F_1^2\left[\gamma\eta_0 + (\tau_- + 2\tau_+)\kappa\eta_0 E_0^2\right]^2\right\}\tau_- = 1. \tag{3}$$

It is obvious from (2) and (3) that, as also happening in the omni-directional scenario, the transmissivities are searched between zero and unity, that is, $\tau_\pm \in [0, 1]$. It is noteworthy that (3) is obtained from (2) if one mutually interchanges the transmissivities (τ_+, τ_-); such a property means that the solutions will appear in pairs leading to the same radiation pattern seen from different perspectives, even if $\tau_+ \neq \tau_-$.

© Author(s) 2021

Once we solve (2) with respect to τ_-, the two (A, B) solutions $\tau_-^{A,B}$ of the quadratic equation (2) read

$$2\tau_-^{A,B} = -\tau_+ - \frac{\gamma\eta_0}{\kappa\eta_0 E_0^2} \pm \frac{1}{F_1|\kappa|\eta_0 E_0^2}\sqrt{\frac{1-\tau_+}{\tau_+}}. \quad (4)$$

Expression A corresponds to the plus (upper) sign and expression B is defined by the minus (lower) sign in (4). By substituting back to (3), one obtains two transcendental equations $G^{A,B}(\tau_+) = 0$, each of which will be solved for steady-state τ_+ within the interval $0 < \tau_+ < 1$. For every single solution of τ_+, we refer back to the corresponding formula (4) for τ_- and, if $0 < \tau_- < 1$, an acceptable set of (τ_+, τ_-) is derived. In this way, the problem of dipolar excitation for a nonlinear metasurface is induced to the (straightforward) detection of real roots of single-variable transcendental functions belonging to a finite range $\tau_\pm \in [0, 1]$. For a linear device ($\kappa = 0$), we obviously find perfect symmetry with respect to the x, y axis ($\cos\varphi$) and thus $\tau_+ = \tau_- = \frac{1}{1+(\gamma\eta_0)^2 F_1^2}$.

C. Alternative polarization

When the magnetic field is parallel to the z axis and the system is excited by a centrally located magnetic current source, the analytical formulation seems more complicated since the electric field determining the nonlinear admittance has two components. However, even in this polarization, for the omni-directional scenario where the incident magnetic field is given by $H_{inc} = \frac{E_0}{\eta_0}\frac{H_0(k_0 r)}{H_1(k_0 a)}$ and transmission ($r > a$) by $H_{tran} = \frac{E_0}{\eta_0} T \frac{H_0(k_0 r)}{H_1(k_0 a)}$, the transmissivity $\tau = |T|^2$ is found to satisfy the following law:

$$\left[1 + F_1^2\left(\gamma\eta_0 + \tau\ \kappa\eta_0 E_0^2\right)^2\right]\tau = 1. \quad (5)$$

It is very similar to that of the other polarization (1) and can be solved analytically, in closed form. Note that we use the expression E_0/η_0 as the input magnetic field magnitude for the obtained results to be directly comparable with those of the other set of waves (of incoming electric field amplitude E_0).

When the nanotube is excited by a magnetic current source of a dipolar pattern, that is, the excitation is written as $H_{inc} = \frac{E_0}{\eta_0}\frac{H_1(k_0 r)}{H_1(k_0 a)}\cos\varphi$ and the output field as $H_{tran} = \frac{E_0}{\eta_0}\frac{H_1(k_0 r)}{H_1(k_0 a)}\left[T_+ e^{+i\varphi} + T_- e^{-i\varphi}\right]$, we follow the same approach and obtain again a nonlinear couple of equations with respect to $\tau_\pm = |T_\pm|^2$ given by

$$\left\{1 + G_1^2\left[4\gamma\eta_0 + 4\frac{\kappa\eta_0 E_0^2}{(k_0 a)^2}\tau_+ + \frac{G_1}{4F_1}\kappa\eta_0 E_0^2(\tau_+ + 2\tau_-)\right]^2\right\}\tau_+ = 1, \quad (6)$$

$$\left\{1 + G_1^2\left[4\gamma\eta_0 + 4\frac{\kappa\eta_0 E_0^2}{(k_0 a)^2}\tau_- + \frac{G_1}{4F_1}\kappa\eta_0 E_0^2(\tau_- + 2\tau_+)\right]^2\right\}\tau_- = 1, \quad (7)$$

where $G_n = \pi k_0 a |H_n'(k_0 a)|^2$ and the prime denotes the derivative with respect to the entire argument. The coupling dynamics are more complicated than the ones captured by (2) and (3); importantly, they differ from each other since (6) and (7) directly involve the optical radius $k_0 a$. Specifically, for thin nanotubes, the autonomous presence of $k_0 a$ enhances the effect of the Kerr coefficient since it appears at the denominator of a fraction whose numerator is proportional to κ. However, the transmissivities (τ_+, τ_-) are again reciprocally exchangeable between (6) and (7). The steady-state solutions can be derived once again via solving (6) with respect to τ_-, that is,

$$2\tau_-^{A,B} = -\tau_+ - \frac{4F_1}{G_1}\left[\frac{4\gamma\eta_0}{\kappa\eta_0 E_0^2} + \frac{4\tau_+}{(k_0 a)^2} \pm \frac{1}{G_1|\kappa|\eta_0 E_0^2}\sqrt{\frac{1-\tau_+}{\tau_+}}\right], \quad (8)$$

and replacing τ_- in (7). In this way, the problem is converted into determining the roots of two transcendental functions across a closed interval $\tau_+ \in [0, 1]$.

III. NUMERICAL SIMULATIONS

A. Omni-directional excitation

By inspection of (1), it is clear that the system is dependent only on the two impedance parameters of the metasurface (γ, κ). In Fig. 2(a), we show the number of real roots of (1) exactly on that plane, and we clearly observe that two domains, symmetric with respect to the origin, correspond to three solutions (brown color) while all the other parametric combinations lead to one unique solution for transmissivity (blue color). Along the line separating the two domains of different colors, either an additional double root emerges (when moving from blue to brown), or solution degeneracy happens (from brown to blue), and thus, two transmissivities are supported. As expected,[34,35] more than one root is found only if the metasurface medium changes its phase when increasing the input intensity E_0^2. In other words, a switch from the dielectric character to plasmonic or vice versa is necessary (but not sufficient), and thus, the signs of the linear admittance and the Kerr coefficient should be opposite ($\gamma\kappa < 0$). Remarkably, when $|\kappa|$ is increasing, the range of (oppositely signed) γ for which three solutions emerge gets more extended. Note finally that when both (γ, κ) are small, the metasurface becomes almost transparent and supports a single solution τ. Quantitatively speaking, the map shown in Fig. 2(a) requires huge electric field

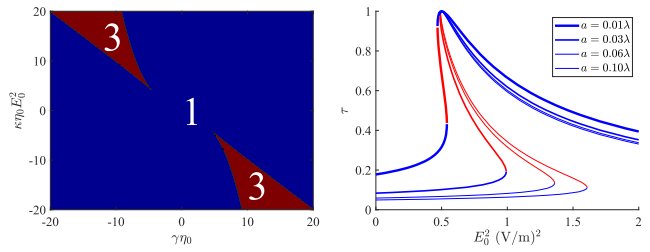

(a) (b)

FIG. 2. (a) Number of acceptable solutions of (1) with respect to transmissivity τ as a function of the linear admittance $\gamma\eta_0$ and the unitless Kerr coefficient $\kappa\eta_0 E_0^2$. When the number is three, we have the appearance of bistability since the third solution is inaccessible and thus unstable ($a = 0.05\lambda$). (b) The S-shaped transmissivity τ as function of incoming intensity E_0^2 for various electrical radii a/λ of the metasurface. The blue color denotes stable, and the red color denotes unstable (inaccessible) solution branches [$\gamma\eta_0 = -10$ and $\kappa\eta_0 = 20(\text{m/V})^2$].

© Author(s) 2021

intensities E_0^2 since the values of Kerr coefficient κ are usually very low. For this reason, several techniques of boosting the nonlinearities, that is, effectively increasing the quantity κ, have been developed. In particular, nonlinear media can be located in the middle of dipole nanoantenna arrays whose resonances amplify the signal locally,[36] assisted by negative refractive index metamaterials combined with strong artificial magnetism to achieve bistable response[37] or sandwiched between epsilon-near-zero plasmonic channels that enhance Kerr effects.[38]

In Fig. 2(b), we present the transmissivity τ as a function of the incoming intensity E_0^2 for various sizes of the nanotube a divided by the operational wavelength λ. One directly notices the S-shaped curves, which reveal bistability; indeed, if the intensity increases from zero, it will reach a critical value where the system will have no alternative but to jump at the upper branch (blue color). Similarly, when the input decreases from a high value, the output will be discontinuous but at an intensity level lower than the previously mentioned one. In this way, a hysteresis loop is formulated, which is the backbone feature in most photonic memory elements; indeed, the system with a specific present excitation E_0^2 will respond differently in proportion to its past values $E_0^2 = E_0^2(t)$. Note that there is always a solution branch that is inaccessible and is called unstable (red color); it makes, therefore, sense that we name this regime bistability despite the presence of three distinct solutions for τ, according to Fig. 2(a).

By inspection of Fig. 2(b), one easily observes that, at a specific level of incoming intensity E_0^2, the transmissivity equals unity ($\tau = 1$) regardless of the size a/λ; obviously, we are talking about $E_0^2 = -\gamma/\kappa$ where the metasurface behaves as totally transparent ($\sigma = 0$). In this way, if different linear admittances or Kerr coefficients are selected, the input E_0^2 for 100% transmission can be controlled at will. When it comes to the S-shaped variation $\tau = \tau(E_0^2)$, the hysteresis loop is more extensive across the E_0^2 axis for larger nanotubes since the developed dynamics are richer and more complex for bigger structures. Note also finally that the linear response can be found by these graphs too by setting $E_0^2 \to 0$; thus, it is clear that the linear transmissivity is inversely correlated with the optical size a/λ of the cylinder.

B. Dipolar excitation

Once the excitation has a dipolar profile, the solution is more complicated since the transmissive field is described by the nonlinear expressions (2) and (3). In Fig. 3(a), we consider a nanotube with $a = 0.05\lambda$, as in Fig. 2(a), and show the number of different transmissivities for each point of the plane $(\gamma\eta_0, \kappa\eta_0 E_0^2)$; one can clearly see that up to nine solutions with $0 < \tau_\pm < 1$ are feasible, contrary to the case shown in Fig. 2(a), where a maximum of three solutions appeared. As in Fig. 2(a), multiple solutions are possible only when $\gamma\kappa < 0$, that is, if the material has the ability of changing its type of response (dielectric/plasmonic). Remarkably, the parameter combinations leading to bistability for the omni-directional excitation of Fig. 2(a) will send the system to a state with as many as nine different solutions for $\tau_\pm$, when excited by dipoles. Into that domain, parametric lobes giving seven non-identical transmissivities emerge while outside of it, the number of potentially supported responses drops to five. When one approaches the boundaries $\gamma = 0$ or $\kappa = 0$, there is a unique solution to the problem, independent from the

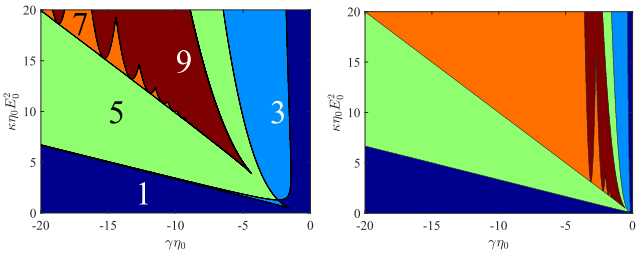

FIG. 3. Number of acceptable solutions of coupled nonlinear equations (2) and (3) with respect to transmissivities (τ_+, τ_-) as a function of the linear admittance $\gamma\eta_0$ and the unitless Kerr coefficient $\kappa\eta_0 E_0^2$. (a) $a/\lambda = 0.05$ and (b) $a/\lambda = 0.005$.

previous values of the excitation, and thus, the operation is memoryless. Note finally the appearance of an almost vertical parametric strip around $\gamma\eta_0 = -3$ corresponding to three distinct solutions.

In Fig. 3(b), we consider a much thinner cylinder ($a = 0.005\lambda$) and show again the number of acceptable solutions of (2) and (3) on the conductivity plane $(\gamma\eta_0, \kappa\eta_0 E_0^2)$. It is noteworthy that the domain corresponding to nine solutions gets substantially shrunk and move toward smaller linear admittances $|\gamma|$, while the scenario of seven distinct transmissivities becomes the dominant one. One may also observe that a system supporting only three different responses is unlikely and, of course, the parametric domains corresponding to the unique solution are similar to these in Fig. 2(b).

In Fig. 4(a), we pick a combination of linear and nonlinear admittance [for $E_0^2 = 3\ (\mathrm{V/m})^2$] that give five distinct transmissivities and represent the function defined by (3) when τ_- is expressed via (4). In this way, two functions of τ_+ are determined, and their variation with respect to τ_+ is shown. We notice that the function obtained with $\tau_- = \tau_-^A$ gives three roots and the other one evaluated with $\tau_- = \tau_-^B$ adds two extra acceptable solutions for τ_+. It should be stressed that τ_-, computed via the corresponding formula (4) for a given root of τ_+, is not necessarily equal to τ_+. Therefore, asymmetric radiation patterns can emerge even if the excitation is symmetric ($\cos\varphi$), due to nonlinearity; similar effects have been

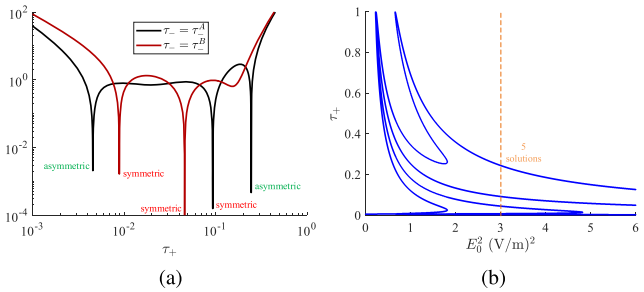

FIG. 4. (a) Function (3) when τ_- is expressed via (4), represented with respect to τ_+. The zeros of the functions correspond to acceptable τ_+. The black curve corresponds to $\tau_- = \tau_-^A$, and the brown curve corresponds to $\tau_- = \tau_-^B$ with $E_0^2 = 3\ (\mathrm{V/m})^2$. (b) The transmissivity τ_+ as a function of incoming intensity E_0^2. The dashed line at $E_0^2 = 3\ (\mathrm{V/m})^2$ crosses the solution branches at the five roots indicated by Fig. 4(a). Plot parameters: $a = 0.05\lambda$, $\gamma\eta_0 = -10$, and $\kappa\eta_0 = 15(\mathrm{m/V})^2$.

© Author(s) 2021

observed owing to gyrotropy.[39,40] In this particular example, the lesser solution $\tau_+ \cong 0.005$ is asymmetric, as shown in Fig. 4(a) since it pairs with $\tau_- \cong 0.25$. Obviously, if the positions between (τ_+, τ_-) are exchanged, that pair constitutes another asymmetric transmissive pattern, as also revealed by the form of (2) and (3); for this reason the number of asymmetric solutions is always even. As it is apparent from Fig. 4(a), the same function originating from each of the two τ_- choices of (4) can have roots corresponding to both symmetric and asymmetric patterns.

In Fig. 4(b), we represent the transmissivity τ_+ for the same design of Fig. 4(a) as a function of incident power E_0^2; the solutions of Fig. 4(a) are found by determining the values of the curve in Fig. 4(b) at the level $E_0^2 = 3\ (\mathrm{V/m})^2$, as indicated by the vertical dashed line. It is remarkable that the variation contains several S-shaped segments, not only one as in Fig. 2(b); in this way, the system permits not two but multiple stable solutions (multistability) and enhances its memory utilities. It should be stressed that $\tau_+ = 1$ occurrs at two different incoming intensities E_0^2 while at least three large hysteresis loops are formed. As predicted by the map of Fig. 3(a), there are ranges of nonlinear admittance $\kappa\eta_0 E_0^2$ (controlled by E_0^2) that make the device support any odd number of solutions, up to nine of them; however, there are combinations of an even number of τ_+ too, but they concern only the boundaries of the corresponding parametric spaces where solution degeneracies happen. In this specific example, the transmissivity is unique for $E_0^2 \to 0$, but beyond a low threshold, multiple (nine) solutions are achievable; when E_0^2 increases further, three different degeneracies gradually occur, and for larger input intensity, the number of different transmissivities τ_+ equals to three.

As shown in Fig. 5(a), we repeat the calculations of Fig. 4(b) for a nanotube of the same size ($a = 0.05\lambda$) but different linear and nonlinear admittances. It is remarkable that for most incoming power levels E_0^2, only a single transmissivity is permitted, and only within a closed interval, three transmissivities are supported, at the ends of which triple roots emerge. One may point out that even in this simple case, bistability is possible if the system is pushed to select another branch when passing from the crossing points. However, there is a clear distinction between the branch that does not exhibit bistability, which gives symmetric patterns obeying the primary excitation ($\cos\varphi$ calling for $\tau_+ = \tau_-$) and a "bubble-like" locus of solutions that break the azimuthal symmetry ($\tau_+ \neq \tau_-$).

The multistability dynamics are much more interesting in Fig. 5(b) where a thinner structure is considered ($a = 0.015\lambda$) for the same admittance profile as that of Fig. 5(a). Again, one directly observes two solution branches: one S-shaped similar to that of Fig. 2(b) along which $\tau_+ = \tau_-$ and another that gives asymmetric radiation patterns ($\tau_+ \neq \tau_-$). Note that the two branches cross each other in several points, and thus, multistability effects, hysteresis loops, and memory properties similar to those indicated by Fig. 5(a) can be also pursued in this setup. However, the most ordinary way for the system to change the solution branch is to be forced to do it, that is, to perform jumps as those shown in Fig. 5(b). Indeed, when one keeps increasing E_0^2 and the system cannot continue across the same solution branch due to root degeneracy, it has no other option but to discontinuously modify its transmissivity. In the depicted example, there are three alternative destinations for that jump: two leading to asymmetric patterns, which are flip mirrored since (τ_+, τ_-) mutually exchange their positions, and one leading to symmetric patterns. We show two transitions—one to symmetric with respect to the x, y axis transmissivity pattern (red color) where the systems continue to work at the S-shaped response curve and another to asymmetric (green color).

In order to better digest the response of the structure, in Fig. 6, we depict the variation in the transmissive field magnitude $|E_{tran}(x,y)|/E_0$ across the xy plane in the two cases indicated by the jumps in Fig. 5(b). In Fig. 6(a), we show the symmetric radiation pattern, and we realize that it is just an attenuated copy of the primary excitation E_{inc}. What is really interesting is that the asymmetric profile shown in Fig. 6(b) is a rotated bipolar distribution. In this way, one can demonstrate sophisticated sensing, switching, and memory features based not only on the magnitude of the bipolar response but also on its rotation angle.

An interesting question that emerges by inspection of Fig. 6 would be "how does the system decide to make transition to the asymmetric or symmetric transmissivity pattern, once the intensity threshold is surpassed?" The truth is that if more than one alternative solution branches exists, the system's choice is dictated by the initial conditions under which it begins to operate. Indeed, each individual point comprising the transmissivity graphs of Figs. 4(b) and 5 corresponds to a constant solution at which the response potentially converges when it reaches its steady state. Every single of the solutions forms parametric regions (basins of attraction) in the phase space of starting points from which the produced fields are attracted by the corresponding steady state as the time goes by. In other words, the exact transitions will be found if one numerically determines

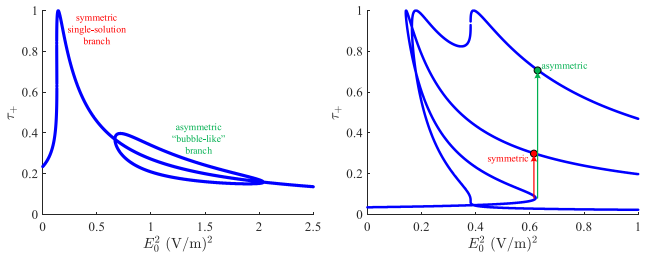

(a) (b)

FIG. 5. Transmissivity τ_+ as a function of incoming intensity E_0^2 for (a) $a = 0.05\lambda$ and (b) $a = 0.015\lambda$. Plot parameters: $\gamma\eta_0 = -1.5$ and $\kappa\eta_0 = 3.5(\mathrm{m/V})^2$.

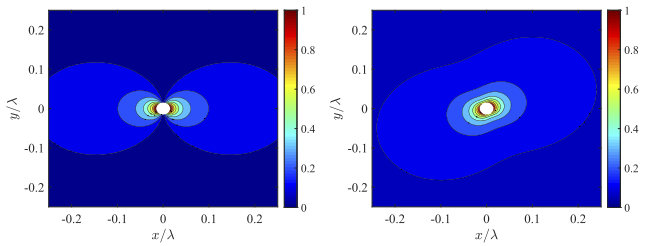

(a) (b)

FIG. 6. Spatial distribution of electric field magnitude $|E_{tran}(x,y)|/E_0$ for the design of Fig. 5(b) at the intensity level $E_0^2 \cong 0.62\ (\mathrm{V/m})^2$, where the discontinuous switch occurs. (a) Symmetric response [indicated by red color in Fig. 5(b)] and (b) asymmetric response [indicated by green color in Fig. 5(b)]. The white disk corresponds to the nanotube cross section.

© Author(s) 2021

the temporal evolution of the nanotube transmissivity, which falls outside the scope of this work; we simply show two indicative discontinuous changes in the response of the structure, assuming that the initial states of the system allow for them. Thorough analyses on the role played by the basins of attraction[41] in nonlinear setups are provided in studies examining a variety of setups including coupled Kerr oscillators,[42] saturable photonic dimers,[43] and nonlinear nanomechanical resonators.[44]

C. Alternative polarization

The system responds differently if excited by the alternative polarization where the magnetic field is parallel to the z axis. As shown in Fig. 7(a), we investigate the transmissivity under omnidirectional illumination, as a function of incoming intensity E_0^2, based on dynamic law (5). The well-known S-shaped curves are formulated for each electrical thickness of the nanotube, and full transmission is observed at the same input power regardless of the radius a/λ since the metasurface becomes transparent ($\sigma = 0$). Importantly, the extent of hysteresis cycle diminishes for bigger cylinders, oppositely to what happens in Fig. 2(b). Another difference in the responses between the two polarizations is that the one considered in Fig. 7(a) needs thicker designs to sustain bistability than the case where the electric field is parallel to the z axis [Fig. 2(a)]. Such a trend has been also met when optimizing similar configurations;[45] indeed, it is the electric field that understands the metasurface effect since it constitutes a dependent source of electric (and not magnetic) current. When the electric field is oriented normally to the rod's axis, it only interacts with its cross section of width $2a$ and demands for more sizable diameters to support a bistable response; this is not the case when the electric field vector is parallel to the axis and "sees" the whole (infinite) cylinder by its oscillation.

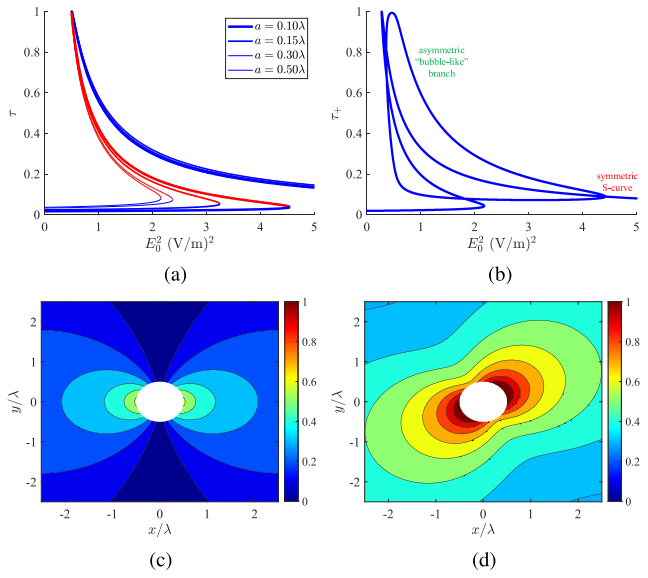

FIG. 7. Structures excited with the alternative polarization, where magnetic field is parallel to z axis. (a) Transmissivity τ as function of input intensity E_0^2 for various sizes of nanotubes a/λ under omni-directional feeding, similar to Fig. 2(b) with $\gamma\eta_0 = -10$ and $\kappa\eta_0 = 20(\mathrm{m/V})^2$. (b) Transmissivity τ_+ as function of input intensity E_0^2 under dipolar feeding, similar to Figs. 4(b), 5(a), and 5(b) with $\gamma\eta_0 = -0.9$ and $\kappa\eta_0 = 4(\mathrm{m/V})^2$. (c) and (d) Spatial distribution of magnetic field magnitude $|H_{tran}(x,y)|/(E_0/\eta_0)$ for the nanotube described in Fig. 7(b). Two different solutions are depicted: one symmetric [such as in Fig. 6(a)] and one asymmetric [such as in Fig. 6(b)] corresponding to the same input intensity $E_0^2 = 0.46\ (\mathrm{V/m})^2$.

In Fig. 7(b), we consider a bipolar source with an axial magnetic field via solving the nonlinear pair of equations (6) and (7), and once again, multistability is observed for the transmissivity of the device when the input intensity E_0^2 is being swept. As in Fig. 5, two families of solutions are formulated: one giving radiation following the excitation azimuthal distribution ($\cos\varphi$, symmetric with respect to the x and y axis) and another producing rotated transmissivity patterns (asymmetric with respect to the x and y axis). The asymmetric-response branch is a closed "bubble-like" loop as found in Fig. 5(a); however, this time, the solution family developing symmetric radiation is bistable by itself, offering the possibility of sharp transitions to multiple values in proportion to the starting point (initial conditions) and the time evolution of the response under causal excitation. In Figs. 7(c) and 7(d), we show the spatial distribution of the normalized radiated magnetic field on the xy plane for two alternative solutions concerning the same input intensity E_0^2, at which the asymmetric branch gives maximal transmissivity.

In Fig. 7(c), we depict the symmetric solution, which is obviously weaker than the asymmetric one appearing in Fig. 7(d); one also observes that the rotation is more substantial than that in Fig. 6(b). Finally, the optical radius of the cylinder is selected quite large, and such a feature is certainly related to the used polarization as indicated by Fig. 7(a) and explained above; in addition, it has to do with the amplifying influence of k_0a on the nonlinearity of the device, as predicted by the coupled dynamics (6) and (7). Indeed, for a very thin nanotube ($k_0a \to 0$), the quantity into the brackets of (6) and (7) increases unboundedly, and in order to give a finite (unitary) product when multiplied by $\tau_\pm$, it inevitably calls for the trivial solution $\tau_+ = \tau_- = 0$.

IV. CONCLUSIONS

A cylindrical metasurface with surface conductivity obeying a simple Kerr-nonlinear law is excited by a line source along its axis either of a circular or bipolar pattern. When the system is fed omnidirectionally, the solution is analytically obtained, and bistability is recorded. On the contrary, to solve the formulated boundary value problem for the dipole source, we drop the terms of higher angular momentum orders, and a coupled nonlinear system is educed. The solutions for transmissivity are obtained by detecting the roots of a transcendental function within a closed interval, and multistability is observed. Importantly, certain solution branches give azimuthally rotated patterns that do not follow the variation of the excitation; in this way, the discontinuous transitions of the response do not concern only the radiated power but also the shape of the transmissive patterns.

An interesting extension of the present work would be to revolutionize the metasurface by admitting it to be not only nonlinear but also active, yielding to a much more interesting and enriched dynamic scheme with reflection-compensation utilities. Of course, when considering structures incorporating gain media, a careful stability analysis is required[46] in order for the transmissivity to be strong but not unboundedly increasing with time. In addition, one may consider multiple concentric metasurfaces[47] characterized by

© Author(s) 2021

inhomogeneous surface admittances[48] via modifying the followed analytical and numerical treatment, to increase the number of stable solutions supported by the system. In this way, the versatility of the device operation as a photonic memory element will be substantially boosted and offer unprecedented capabilities of tunable storage and reconfigurable information encryption.

ACKNOWLEDGMENTS

This work was supported financially by Nazarbayev University Faculty Development Competitive Research Grant No. 021220FD4051 ("Optimal Design of Photonic and Quantum Metamaterials").

The authors would like to thank Mr. Aidynbek Tussipzhan (Nazarbayev University, Kazakhstan) for useful discussions during the early stages of this work.

DATA AVAILABILITY

The data that support the findings of this study are available within the article.

REFERENCES

[1] R. W. Boyd, *Nonlinear Optics*, 3rd ed. (Academic Press, Orlando, FL, 2008).
[2] Y. Kivshar and G. Agrawal, *Optical Solitons: From Fibers to Photonic Crystals* (Academic Press, New York, 2003).
[3] S. Keren-Zur, L. Michaeli, H. Suchowski, and T. Ellenbogen, "Shaping light with nonlinear metasurfaces," Adv. Opt. Photonics **10**, 309–353 (2018).
[4] T. Brabec and F. Krausz, "Intense few-cycle laser fields: Frontiers of nonlinear optics," Rev. Mod. Phys. **72**, 545 (2000).
[5] Y. Akahane, T. Asano, B.-S. Song, and S. Noda, "High-Q photonic nanocavity in a two-dimensional photonic crystal," Nature **425**, 944–947 (2003).
[6] N. Segal, S. Keren-Zur, N. Hendler, and T. Ellenbogen, "Controlling light with metamaterial-based nonlinear photonic crystals," Nat. Photonics **9**, 180–184 (2015).
[7] J. Lee, M. Tymchenko, C. Argyropoulos, P.-Y. Chen, F. Lu, F. Demmerle, G. Boehm, M.-C. Amann, A. Alù, and M. A. Belkin, "Giant nonlinear response from plasmonic metasurfaces coupled to intersubband transitions," Nature **511**, 65–69 (2014).
[8] Y. Yang, W. Wang, A. Boulesbaa, I. I. Kravchenko, D. P. Briggs, A. Puretzky, D. Geohegan, and J. Valentine, "Nonlinear fano-resonant dielectric metasurfaces," Nano Lett. **15**, 7388–7393 (2015).
[9] J. Leuthold, C. Koos, and W. Freude, "Nonlinear silicon photonics," Nat. Photonics **4**, 535–544 (2010).
[10] M. Kauranen and A. V. Zayats, "Nonlinear plasmonics," Nat. Photonics **6**, 737–748 (2012).
[11] N. C. Panoiu, W. E. I. Sha, D. Y. Lei, and G.-C. Li, "Nonlinear optics in plasmonic nanostructures," J. Opt. **20**, 083001 (2018).
[12] I. Liberal and N. Engheta, "Near-zero refractive index photonics," Nat. Photonics **11**, 149–158 (2017).
[13] M. Chen, K. A. Rubin, and R. W. Barton, "Compound materials for reversible, phase-change optical data storage," Appl. Phys. Lett. **49**, 502 (1986).
[14] Y. Yang, J. Ouyang, L. Ma, R. J.-H. Tseng, and C.-W. Chu, "Electrical switching and bistability in organic/polymeric thin films and memory devices," Adv. Funct. Mater. **16**, 1001–1014 (2006).
[15] B. F. Soares, F. Jonsson, and N. I. Zheludev, "All-optical phase-change memory in a single gallium nanoparticle," Phys. Rev. Lett. **98**, 153905 (2007).
[16] M. Salinga, B. Kersting, I. Ronneberger, V. P. Jonnalagadda, X. T. Vu, M. Le Gallo, I. Giannopoulos, O. Cojocaru-Mirédin, R. Mazzarello, and A. Sebastian, "Monatomic phase change memory," Nat. Mater. **17**, 681–685 (2018).
[17] M. Wuttig, H. Bhaskaran, and T. Taubner, "Phase-change materials for non-volatile photonic applications," Nat. Photonics **11**, 465–476 (2017).
[18] X. Li, N. Youngblood, C. Ríos, Z. Cheng, C. D. Wright, W. H. Pernice, and H. Bhaskaran, "Fast and reliable storage using a 5 bit, nonvolatile photonic memory cell," Optica **6**, 1–6 (2019).
[19] Z. Huang, A. Baron, S. Larouche, C. Argyropoulos, and D. R. Smith, "Optical bistability with film-coupled metasurfaces," Opt. Lett. **40**, 5638–5641 (2015).
[20] M. Zhang, M. Pu, F. Zhang, Y. Guo, Q. He, X. Ma, Y. Huang, X. Li, H. Yu, and X. Luo, "Plasmonic metasurfaces for switchable photonic spin-orbit interactions based on phase change materials," Adv. Sci. **5**, 1800835 (2018).
[21] A. Nicolas, L. Veissier, L. Giner, E. Giacobino, D. Maxein, and J. Laurat, "A quantum memory for orbital angular momentum photonic qubits," Nat. Photonics **8**, 234–238 (2014).
[22] B. Romeira, R. Avó, J. M. L. Figueiredo, S. Barland, and J. Javaloyes, "Regenerative memory in time-delayed neuromorphic photonic resonators," Sci. Rep. **6**, 19510 (2016).
[23] A. M. Morsy, R. Biswas, and M. L. Povinelli, "High temperature, experimental thermal memory based on optical resonances in photonic crystal slabs," APL Photonics **4**, 010804 (2019).
[24] P. J. Pauzauskie and P. Yang, "Nanowire photonics," Mater. Today **9**, 36–45 (2006).
[25] D. Wei, C. Wang, X. Xu, H. Wang, Y. Hu, P. Chen, J. Li, Y. Zhu, C. Xin, X. Hu, Y. Zhang, D. Wu, J. Chu, S. Zhu, and M. Xiao, "Efficient nonlinear beam shaping in three-dimensional lithium niobate nonlinear photonic crystals," Nat. Commun. **10**, 4193 (2019).
[26] R. Li, H. Wang, B. Zheng, S. Dehdashti, E. Li, and H. Chen, "Bistable scattering in graphene-coated dielectric nanowires," Nanoscale **9**, 8449–8457 (2017).
[27] T. Naseri, N. Daneshfar, and F. Pourkhavari, "Investigation of optical bistability in core-shell nanoparticles consisting of nonlocal core and magnetoplasmonic shell," Phys. Plasmas **25**, 082304 (2018).
[28] Y.-S. Du and J.-Y. Yan, "Plasmonic bistability in the nonlinear cylindrical metal-dielectric multilayers," J. Appl. Phys. **116**, 104305 (2014).
[29] Y. Huang, Y. M. Wu, and L. Gao, "Nonlocality-broaden optical bistability in a nonlinear plasmonic core-shell cylinder," J. Phys. Chem. C **121**, 8952–8960 (2017).
[30] A. Karnieli, S. Trajtenberg-Mills, B. Boulanger, and A. Arie, "Modified quasi-phase-matching and spectral shaping in a nonlinear whispering gallery mode resonator," J. Opt. Soc. Am. B **34**, 1971–1980 (2017).
[31] S. Caorsi, A. Massa, and M. Pastorino, "Approximate solutions to the scattering by nonlinear isotropic dielectric cylinders of circular cross sections under TM illumination," IEEE Trans. Antennas Propag. **43**, 1262–1269 (1995).
[32] A. Mirzaei, A. E. Miroshnichenko, N. A. Zharova, and I. V. Shadrivov, "Light scattering by nonlinear cylindrical multilayer structures," J. Opt. Soc. Am. B **31**, 1595–1599 (2014).
[33] C. A. Valagiannopoulos, M. S. Mirmoosa, I. S. Nefedov, S. A. Tretyakov, and C. R. Simovski, "Hyperbolic-metamaterial antennas for broadband enhancement of dipole emission to free space," J. Appl. Phys. **116**, 163106 (2014).
[34] M. Wuttig and N. Yamada, "Phase-change materials for rewriteable data storage," Nat. Mater. **6**, 824–832 (2007).
[35] H.-S. P. Wong, S. Raoux, S. Kim, J. Liang, J. P. Reifenberg, B. Rajendran, M. Asheghi, and K. E. Goodson, "Phase change memory," Proc. IEEE **98**, 2201–2227 (2010).
[36] P.-Y. Chen and A. Alù, "Optical nanoantenna arrays loaded with nonlinear materials," Phys. Rev. B **82**, 235405 (2010).
[37] P.-Y. Chen, M. Farhat, and A. Alù, "Bistable and self-tunable negative-index metamaterial at optical frequencies," Phys. Rev. Lett. **106**, 105503 (2011).
[38] C. Argyropoulos, P.-Y. Chen, G. D'Aguanno, N. Engheta, and A. Alù, "Boosting optical nonlinearities in ϵ-near-zero plasmonic channels," Phys. Rev. B **85**, 045129 (2012).
[39] C. Valagiannopoulos, S. A. H. Gangaraj, and F. Monticone, "Zeeman gyrotropic scatterers: Resonance splitting, anomalous scattering, and embedded eigenstates," Nanomater. Nanotechnol. **8**, 1 (2018).
[40] S. A. H. Gangaraj, C. Valagiannopoulos, and F. Monticone, "Topological scattering resonances at ultralow frequencies," Phys. Rev. Res. **2**, 023180 (2020).

© Author(s) 2021

[41] J. M. T. Thompson and H. B. Stewart, *Nonlinear Dynamics and Chaos* (Willey & Sons, New York, 2002).
[42] I. Sliwa and K. Grygiel, "Periodic orbits, basins of attraction and chaotic beats in two coupled Kerr oscillators," Nonlinear Dyn. **67**, 755–765 (2012).
[43] Y. Zhiyenbayev, Y. Kominis, C. Valagiannopoulos, V. Kovanis, and A. Bountis, "Enhanced stability, bistability, and exceptional points in saturable active photonic couplers," Phys. Rev. A **100**, 043834 (2019).
[44] I. Kozinsky, H. W. Ch. Postma, O. Kogan, A. Husain, and M. L. Roukes, "Basins of attraction of a nonlinear nanomechanical resonator," Phys. Rev. Lett. **99**, 207201 (2007).
[45] A. Abrashuly and C. Valagiannopoulos, "Limits for absorption and scattering by core-shell nanowires in the visible spectrum," Phys. Rev. Appl. **11**, 014051 (2019).
[46] B. Yerezhep and C. Valagiannopoulos, "Approximate stability dynamics of concentric cylindrical metasurfaces," IEEE Trans. Antennas Propag. **11**, 014051 (2019).
[47] C. A. Valagiannopoulos and P. Alitalo, "Electromagnetic cloaking of cylindrical objects by multilayer or uniform dielectric claddings," Phys. Rev. B **85**, 115402 (2012).
[48] C. A. Valagiannopoulos, "Arbitrary currents on circular cylinder with inhomogeneous cladding and RCS optimization," J. Electromagn. Waves Appl. **21**, 665–680 (2007).

© Author(s) 2021